Delft University of Technology

Thermal Crosstalk of X-Ray Transition-Edge Sensor Micro-Calorimeters under Frequency Domain Multiplexing Readout

Vaccaro, Davide; Akamatsu, Hiroki; Bruijn, Marcel; Gottardi, Luciano; Den Hartog, Roland; Van Der Kuur, Jan; Ridder, Marcel; De Wit, Martin; Gao, Jian Rong; More Authors

Citation (APA)
Vaccaro, D., Akamatsu, H., Bruijn, M., Gottardi, L., Den Hartog, R., Van Der Kuur, J., Ridder, M., De Wit, M., Gao, J. R., & More Authors (2022). Thermal Crosstalk of X-Ray Transition-Edge Sensor Micro-Calorimeters under Frequency Domain Multiplexing Readout. *IEEE Transactions on Applied Superconductivity*, *32*(1). https://doi.org/10.1109/TASC.2021.3128710

Important note
To cite this publication, please use the final published version (if applicable).
Please check the document version above.

Thermal Crosstalk of X-Ray Transition-Edge Sensor Micro-Calorimeters Under Frequency Domain Multiplexing Readout

Davide Vaccaro ⓘ, Hiroki Akamatsu, Marcel Bruijn, Luciano Gottardi ⓘ, Roland den Hartog, Jan van der Kuur ⓘ, Ton van der Linden, Kenishiro Nagayoshi, Kevin Ravensberg, Marcel Ridder, Emanuele Taralli, Martin de Wit ⓘ, Jian-Rong Gao ⓘ, Ruud Hoogeveen, and Jan-Willem den Herder

Abstract—We have measured and characterized the thermal crosstalk in two different arrays of transition-edge sensor (TES) X-ray microcalorimeters with frequency-domain multiplexing (FDM) readout. The TES arrays are fabricated at SRON and are a 8×8 and a 32×32 "kilo-pixel" uniform array. The amount of crosstalk is evaluated as the ratio between the averaged crosstalk signal and the X-ray pulse amplitudes. The crosstalk ratios (CRs) for our detectors are compliant with the requirements for future X-ray space missions, such as Athena X-IFU (CR $< 10^{-3}$ for first-neighbor pixels): We measured a nearest neighbor thermal CR at a level of 10^{-4}, with a highest CR of 4×10^{-4} for the kilo-pixel array (worst case, center of array) and 1×10^{-4} for the 8×8 array, with a margin of improvement achievable by optimizing the Cu metallization and the width of the Si supporting structures (muntins) in the backside of the TES array chip. Based on the measured CRs, we have estimated the impact on the spectral resolution by means of noise equivalent power considerations and a Monte Carlo simulation, finding an average degradation in quadrature of less than 40 meV, compliant with the <0.2 eV requirement for Athena X-IFU.

Index Terms—detector energy resolution, frequency domain multiplexing, monte carlo, space-borne satellites, transition-edge sensors, thermal crosstalk, X-ray micro-calorimeters, x-ray astronomy.

I. INTRODUCTION

TRANSITION-EDGE sensors [1] (TESs) are very sensitive devices used as bolometers or single-photon microcalorimeters in a variety of present and future astrophysical missions, such as LiteBIRD [2], HUBS [3], and Athena X-IFU [4]. Given the stringent limitations of spaceborne missions in terms of available cooling power at sub-*K* temperatures, the readout of TESs is usually performed under a multiplexing scheme. Several multiplexing methods exist, whose means are to modulate the detector signals with a set of orthogonal carriers within a limited bandwidth and perform their transmission via a common line.

At SRON, we are developing large, close-packed arrays of TES bolometers for sub-mm and far-IR observatories and microcalorimeters for X-ray astronomy. To perform their readout, we have been developing a frequency-domain multiplexing (FDM) technology with base-band feedback [5] (BBFB).

In our FDM readout for X-ray microcalorimeters, the voltage bias for the TESs is provided by a comb of sinusoidal carriers generated by a custom warm electronics board (DEMUX). A tuned, high-Q *LC* bandpass filter is placed in series with each detector, limiting the information bandwidth and allowing only one frequency from the carrier comb to provide the ac bias. An X-ray releasing energy in a TES causes its temperature and resistance to increase and its current to drop, and then electro-thermal feedback (ETF) brings the system back to its original point, resulting in an amplitude-modulation of the signal. The TESs' output currents are summed at the input port of a superconducting quantum interference device (SQUID). An analog low-noise amplifier provides a further amplification at room temperature before the analog-to-digital conversion in the DEMUX board, where demodulation is performed to recover the X-ray signal. In the BBFB scheme, the demodulated signals are remodulated and fed back to the SQUID via the feedback line, after compensating for the delay due to transmission time, to null the SQUID output. This effectively increases the available dynamic range and allows for a large multiplexing factor (i.e., number of pixels per readout chain). In our case, the FDM readout is performed in the bandwidth from 1 to 5 MHz with a pixel separation of 100 kHz. For more details on the scheme and the most recent demonstration of our FDM readout for X-ray TES microcalorimeters, see the study from Akamatsu *et al.* [6].

Given the proximity of the pixels both physically and in frequency space, the spectral resolution of the detectors is

susceptible to crosstalk. We observe two types of crosstalk: thermal crosstalk (TCT) and electrical crosstalk (ECT). When dealing with crosstalk between two pixels, we call the "Perpetrator" the pixel where an actual X-ray event is detected and the "Victim" the pixel where a spurious signal due to crosstalk is observed.

TCT occurs because a part of the energy deposited by an X-ray in the Perpetrator pixel is not compensated via the ETF mechanism, i.e., by the reduction in Joule heating dissipated by the TES. As such, the level of TCT depends on the effective strength of ETF, quantified by the loop gain $\mathcal{L}$

$$\mathcal{L} = \frac{\alpha}{n}\left[1 - \left(\frac{T_b}{T}\right)^n\right]\frac{1 - R_s/R}{1 + R_s/R + \beta} \qquad (1)$$

where R_s and R are the shunt resistance and TES resistance, n is the thermal conductance exponent (for the detectors used in our experiments, $n \approx 3.2$), T_b and T are the bath temperature and TES temperature, and $\alpha \equiv d(\ln R)/d(\ln T)$ and $\beta \equiv d(\ln R)/d(\ln I)$ are the TES temperature and current sensitivity, respectively. If an amount of energy E_0 is deposited by an X-ray in the Perpetrator, a fraction $E_0/(1 + \mathcal{L})$ is not compensated by a reduction of Joule heating of the TES and dissipates into the thermal bath, becoming a source of TCT. TCT can then be minimized by proper heat-sinking of the array. We usually bias our devices along the transition at $R = 20\%$ of the normal resistance, where typically $\alpha \sim 500$ and $\beta \sim 5$, resulting in $\mathcal{L} \sim 25$ (the values for other quantities necessary for $\mathcal{L}$ calculation are given in Section II).

ECT occurs when the electrical signal in the readout chain produced by the detection of an X-ray in the Perpetrator pixel causes a spurious signal to be observed in the Victim pixel. ECT does not originate from the detector array but merely from the readout circuit. There are several factors that can produce ECT in an FDM system, such as carrier leakage, common inductance in the ac bias line and/or at the SQUID input line, or mutual inductance between neighbor inductors in the LC filter chip.

In this article, we present an experimental characterization of TCT for two different TES arrays fabricated at SRON, using two of our FDM setups, namely the XFDM setup and the kilo-pixel setup (described in next section). ECT is not the main focus of the article and is not treated.

This article is structured as follows. In Section II, we describe the TES arrays and the FDM setups used for the measurements. The experimental approach is explained in Section III and the results are discussed in Section IV. Finally, Section V concludes this article.

II. EXPERIMENTAL SETUP

To give a better overview on the two setups, the detector parameters and readout components described below are also summarized in Table I.

A. TES Arrays

The detectors used in the experiments reported in this article have been developed at SRON. The arrays used in the two setups have both different devices and different layout. The XFDM setup hosts a 8×8 uniform array, 32 TESs of which are connected to the readout circuit. The kilo-pixel setup hosts a 32×32 uniform kilo-pixel array, 38 TESs of which are connected to readout circuit.

TABLE I
SUMMARY OF THE TES AND READOUT PARAMETERS FOR
THE TWO FDM SETUPS

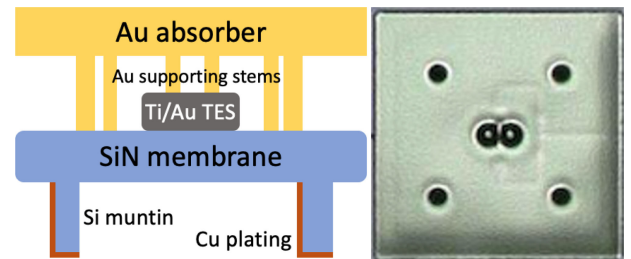|	XFDM	kilo-pixel
TES design	$50\mathrm{x}10\ \mu\mathrm{m}^2$	$80\mathrm{x}20\ \mu\mathrm{m}^2$
TES array	8×8, 32 connected	32×32, 38 connected
R_N	125 mΩ	100 mΩ
T_C	85 mK	85 mK
G @ T_C	50 pW/K	80 pW/K
C @ 90 mK	0.85 pJ/K	0.85 pJ/K
L_{eff}	3.7 μH	2.8 μH
R_s	1 mΩ	1 mΩ
T_b	55 mK	53 mK

Fig. 1. Left: not-to-scale sketch for a single pixel. Right: microscope top-view picture of a single pixel ($240 \times 240\ \mu\mathrm{m}^2$, 250 μm pitch), with the gold absorber and the six supporting stems in evidence and the Nb leads for the TES readout visible underneath.

Each TES consists of a Ti/Au bilayer deposited on a 500-nm thick SiN membrane. The bilayer dimensions are $50 \times 10\ \mu\mathrm{m}^2$ and $80 \times 20\ \mu\mathrm{m}^2$ for the array hosted in the XFDM and kilo-pixel setup, respectively. The bilayer is coupled to a $240 \times 240\ \mu\mathrm{m}^2$, 2.3-$\mu$m thick Au absorber (heat capacity $C = 0.85$ pJ/K at 90 mK) via two central pillars, with four additional corner stems providing mechanical support, as shown in Fig. 1, right plot. The $50 \times 10\ \mu\mathrm{m}^2$ devices have critical temperature $T_C \simeq 85$ mK, normal resistance $R_N \simeq 125$ mΩ, and thermal conductance $G \sim 50$ pW/K at T_C. The $80 \times 20\ \mu\mathrm{m}^2$ devices have $T_C \simeq 85$ mK, $R_N \simeq 100$ mΩ, and $G \sim 80$ pW/K at T_C.

Thermalization of the TES chip is provided by Au wire-bondings between the Cu sample holder and the gold layer on top of the array. To further improve the thermal contact, a 1-μm Cu layer with 20-nm Au capping is added to the Si supporting structures (muntins) on the backside of the chip. The width of the muntins for this batch of arrays is 60 μm. Due to the position and orientation of the sample holder inside the evaporation chamber, the muntins are not uniformly metallized, as shown in Fig. 1, left plot.

For further details about the TES array fabrication, see the study from Nagayoshi *et al.* [7]. For further details about their ac operation and spectral performance, see the study from de Wit *et al.* [8].

B. FDM Setups

In both the XFDM and kilo-pixel setups, the TESs are coupled to custom LC filters [9] and superconducting transformers for impedance matching, resulting in an effective inductance of 3.7 and 2.8 μH for the XFDM and kilo-pixel setup, respectively. The voltage bias is obtained through a 750-m Ω surface mount
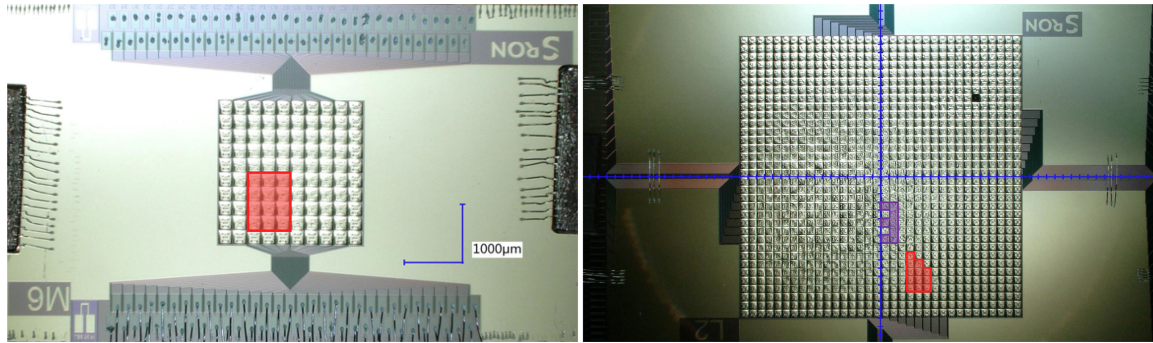
Fig. 2. TES arrays used in the XFDM setup (left) and kilo-pixel setup (right). The colored area (purple = center of array, red = edge of array) represents the pixels activated during the crosstalk measurements.

device resistor and a capacitive divider with a 1:26 ratio, for an effective shunt resistance $R_s \simeq 1$ mΩ. The TES summed signals are preamplified at cryogenic stage via two SQUIDs (VTT model J3 as front-end and VTT model F5 as amplifier). Such "cold" components are hosted on custom oxygen-free high-conductivity (OFHC) copper and enclosed in a niobium shield. Superconducting Helmolz coils are employed to cancel out residual stray magnetic field after the cooldown. The detectors are hit with 5.9-keV X-rays produced from an ^{55}Fe source hosted on the Nb magnetic shield. Aluminum foils are employed in front of the X-ray source to adjust the count rate to ∼1 count per second per pixel. A copper collimator is placed just above the TES array to avoid nonbiased pixels being hit, as these lack the ETF and thus would cause thermal fluctuations in the array.

The setups are both housed in the same cryo-cooler, a Leiden Cryogenics dilution unit with a cooling power of 400 μW at 120 mK. The setups are hanged via Kevlar wires to the mixing chamber to damp mechanical oscillations [10]. OFHC copper braids connecting the setups to the mixing chamber ensure the thermal anchoring. The setups' temperatures are controlled and monitored via a Ge thermistor anchored to the copper holder. For the measurements reported in this article, the base temperature for the XFDM setup is 55 mK and for the kilo-pixel setup is 53 mK.

III. EXPERIMENTAL APPROACH

To evaluate the amount of crosstalk, we simultaneously activate N neighbor pixels and bias them at ≈20% of their superconducting transition, where the best spectral performances are observed. In Fig. 2, we show the smaller 8×8 array and the larger kilo-pixel array and the map of pixels activated during the experiments.

When one pixel is triggered by an X-ray event, data for all the active pixels is stored. The total events number is chosen to sufficiently reduce the noise floor (scaled to the amplitude of an X-ray pulse) to a level of ≈10^{-5}. This number is chosen based on preliminary measurements [11] which showed the scaled amplitude of the TCT signal to be at a level of 10^{-4} or higher. In this way, a total of $N \times 5000$ events is acquired. We cannot, however, control the precise number of events acquired per each individual pixel.

Since we are activating multiple pixels, intermodulation distortions from nonlinearities in the readout chain are expected to produce spurious line noises within the TES sensitive bandwidth. To avoid this, we use a frequency shift algorithm [12],
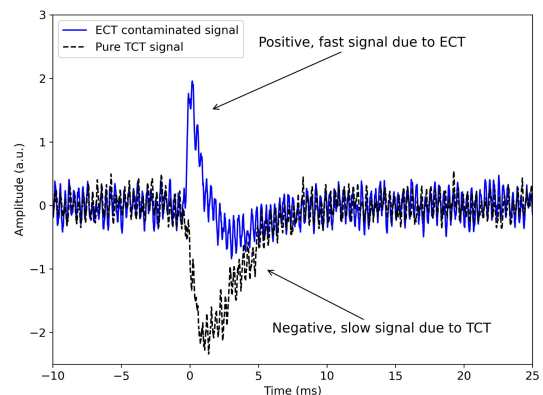

Fig. 3. Example of ECT contaminated signal (blue) and pure TCT signal (black dashed) for the same Victim pixel of Fig. 5.

[13] to shift in frequency space the intermodulation lines and place them sufficiently far away from the sensitive bandwidth of the TES.

To estimate the crosstalk ratio (CR) between the Victim pixel and the neighboring Perpetrator pixels, we first construct the averaged X-ray pulse and TCT pulse for the Victim pixel. The average X-ray pulse is calculated by taking the average of the collected X-ray pulses, excluding those events which contain more than one pulse within the recorded event length. To analyze the data, we first subtract the baseline and take the absolute value of the amplitude to change the polarity of the pulse to positive. Then, for each Victim–Perpetrator pair, the average TCT pulse is calculated by averaging the signals for the Victim pixel acquired when the data acquisition was triggered by an X-ray in the Perpetrator pixel. The crosstalk ratio CR is then evaluated as

$$\mathrm{CR} = \frac{\overline{A}_{\mathrm{tct}}}{A_x} \qquad (2)$$

where $\overline{A}_{\mathrm{tct}}$ is the amplitude of the TCT pulse averaged on 10 points (≈64 μs in time scale) around the maximum and A_x is the peak value of the X-ray pulse.

Both the TCT and X-ray pulse in this calculation refer to the Victim pixel. Ideally, the TCT pulse amplitude should be referred to the source X-ray pulse, which would require biasing the detectors from a perfectly uniform array on the same bias point (hence, same α and β) and having the same gain of readout electronics. In our ac case, the bias of each TES is performed
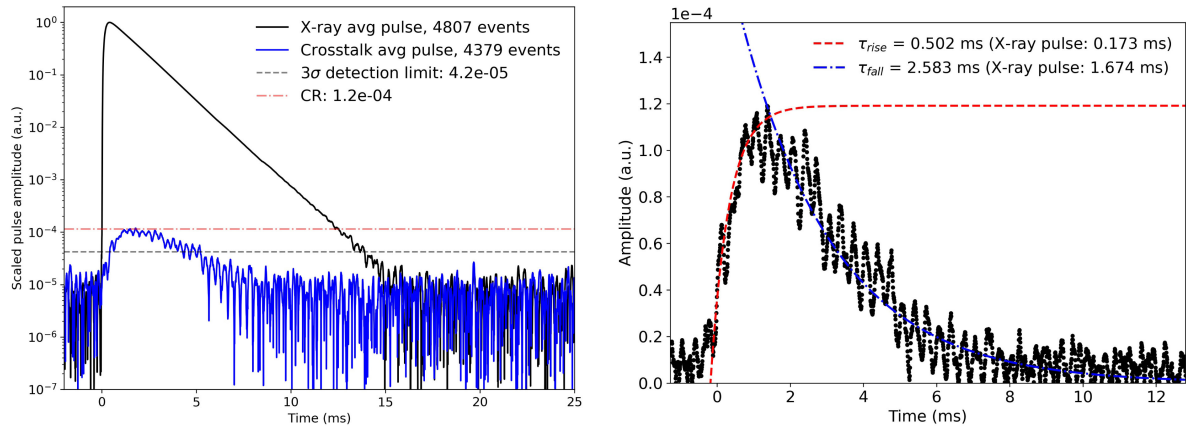
Fig. 4. Example of crosstalk processed data, obtained from the XFDM setup. Left: comparison between the average 5.9-keV X-ray from the Mn-K α line of the ^{55}Fe source detected by the Victim (black) and the averaged TCT signal in the Victim (blue) caused by X-ray events in a nearest neighbor Perpetrator. Right: fit of the rise time and fall time for the TCT pulse. The amplitudes are normalized to the pulse height of the average X-ray pulse. The slew rate of the X-ray pulses is at a level of 150 mA/s.

independently, which allows to tune the bias voltage individually to obtain the best performance for each pixel but, also due to the presence of weak link effect [16] and the total gain of the readout electronics not being constant across the FDM bandwidth, makes it not straightforward to exactly bias to the same bias point. Therefore, calculating the CR using the X-ray pulse from the source pixel as reference would lead to a mis-estimation.

During the analysis, we observed data contaminated by ECT (an example is shown in Fig. 3), whose signatures are 1) the opposite polarity of the signal and 2) the faster rise time and fall time since it is caused by the parasitic inductive coupling within the readout circuit and not by a thermo-electrical effect. In our FDM systems, the main cause of ECT is the common inductance in the ac bias and SQUID feedback line so that the amount of ECT is proportional to $\omega/\Delta\omega$, where ω is the bias frequency of the Victim pixel and $\Delta\omega$ is the bias frequency difference between the Victim and the Perpetrator. ECT can be improved by reducing the length of the common paths in the ac bias and SQUID feedback line, consisting of lithographed strip-lines and Al bonding wires. For the results that follow, Victim–Perpetrator pairs contaminated from ECT are discarded from the analysis so that the events analyzed refer to pure TCT.

IV. RESULTS AND DISCUSSION

A. Crosstalk Ratios

In Fig. 4, left plot, we show an example of processed data for TCT. From the noise floor level, we define a 3σ detection threshold, where σ is calculated as the root mean square of the noise floor level. We deem TCT detection and proceed with the CR calculation if two conditions are met: 1) the averaged crosstalk pulse shape has the proper polarity (ECT rejection) and 2) the TCT pulse amplitude is above the 3σ detection threshold.

For Victim–Perpetrator pairs with relative distance of two pixels or more however, the observed TCT signals are low enough to make the 3σ criterion too stringent: For those pairs, condition 2) is replaced with condition 3) and the integral of the TCT pulse is at least 30% larger than the integral of the noise floor, where the integrals are considered in the time interval where the detected pulse signal is above the noise floor (typically few milliseconds). The threshold of 3σ of condition 2) and the use of condition 3)
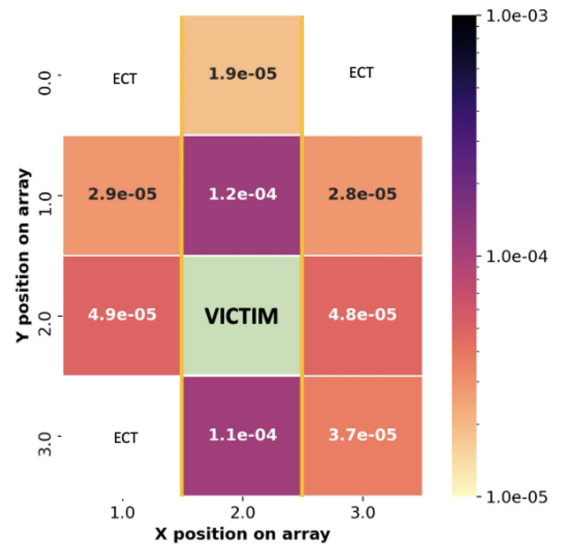

Fig. 5. Example of crosstalk heatmap for one Victim pixel in the XFDM setup, constructed according to the geometrical distribution of the active pixels in the array. The numbers represent the crosstalk ratios measured for the corresponding Perpetrator pixel toward the Victim pixel. The gold-colored vertical bars in the left plot represent the area where the Cu metallization is expected to be on the silicon muntins. The color bar is scaled up to the requirement for Athena X-IFU for crosstalk between nearest neighbors ($=10^{-3}$). Perpetrators whose major source of crosstalk toward the Victim was ECT are excluded from the analysis.

are a compromise to effectively prevent false detection and at the same time avoiding to reject data points at pixel distances of 2 or higher, where the measured CRs are small. The cost is that, for pixel distances of 2 or more, the error bar (= detection threshold $\approx 2 \times 10^{-5}$) on the CR value is significant.

Due to the higher ECT in the kilo-pixel setup (due to longer wire-bonds in the ac bias and SQUID input lines), a larger number of Perpetrator–Victim pairs is excluded from the analysis than in the XFDM case. We separately fit the rising and falling flank of the TCT pulses with a single exponential function to extract the rise and fall times, as shown in Fig. 4, right plot. The information about the X-ray pulse time scale is used for the Monte Carlo simulation in Section IV-B2.
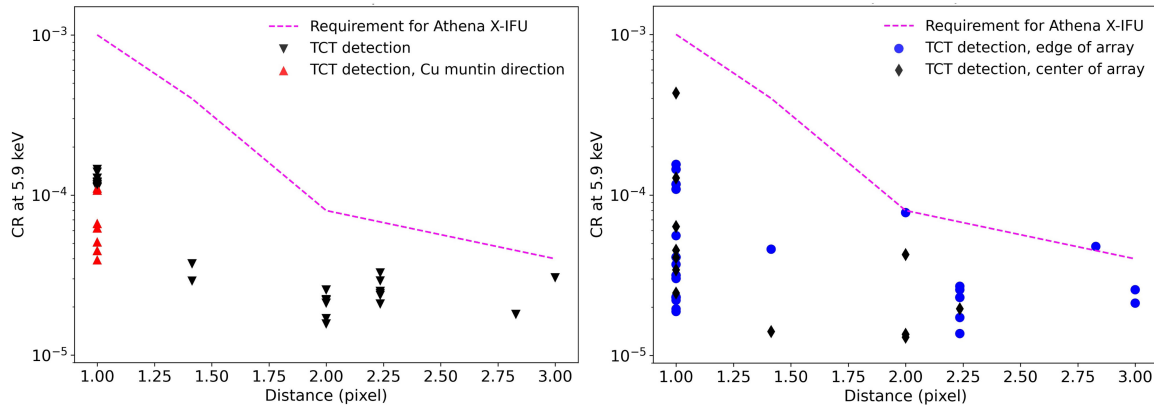
Fig. 6. Crosstalk ratios as a function of distance between pixels for all the Victim–Perpetrator combinations for the XFDM setup (left) and kilo-pixel setup (right). As a reference, we compare our results with the requirement for Athena X-IFU. Data with ECT contamination is excluded. The uncertainty on CR for each data point is at a level of 2×10^{-5}. The error bars are not shown for plot clarity.

We then produce TCT maps for each pixel of the array. Fig. 5 shows an example of such a map, as measured in the XFDM setup (left plot) and kilo-pixel setup (middle and right plots). We construct a map for each Victim in the array: In this way, we correlate the measured CR with the relative distance between the Victim and the Perpetrator pixel, as shown in Fig. 6.

We observe a directional dependency in CR for nearest neighbor pixels, which we interpret as the effect of the nonuniform copper metallization of the silicon muntins, which in turn depends on the position and orientation of the array on the fabrication mask. This effect is more clear for the XFDM setup: A nearest-neighbor Perpetrator pixel lying in the Victim pixel in the direction of the Cu-plated muntin produces a TCT which is significantly lower than for Perpetrator and Victim lying in the direction on muntin without deposited copper.

Taking as reference the requirements for Athena X-IFU [15], we observe that the amount of crosstalk for our array is at acceptable levels, with highest CRs of 1.4×10^{-4} in the XFDM setup, and for the kilo-pixel setup 1.6×10^{-4} at edge of array and 4.3×10^{-4} in the center of the array. These values are expected to be improved in future batches of arrays, envisaging a larger width of the silicon muntins (from 60 to 85 μm) and a uniform Cu metallization.

B. Impact on Spectral Performance

Having measured the level of TCT for our TES arrays, we want to estimate its impact on the spectral performance of the detectors. To do so, we adopt two approaches: 1) estimation from noise equivalent power (NEP) and 2) Monte Carlo simulation.

1) Estimation From NEP: TCT can be considered as a disturbance in the thermal stability of the TES. In this sense, as done in the study by Iyomoto *et al.* [17], we can estimate the impact on energy resolution via the integrated NEP, defined as

$$\Delta E = 2.335 \times \left(\int_0^\infty \frac{4}{\mathrm{NEP}(f)^2} df \right)^{-1/2} \quad (3)$$

where 2.335 is the conversion factor from rms to FWHM, f is the frequency, and $\mathrm{NEP}(f)$ is the NEP spectrum, defined as the ratio of the average noise power spectral density to the normalized detector responsivity, which we calculate from the average 6 keV X-ray pulse spectrum normalized to power units.
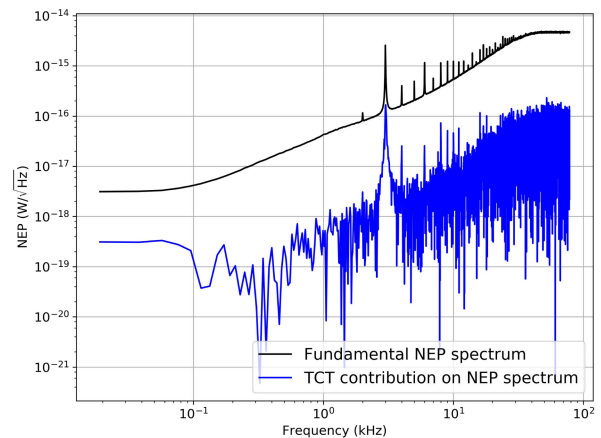

Fig. 7. Example of measured NEP spectrum calculated only with the fundamental noise of the detector (black) and the contribution in quadrature of the thermal crosstalk induced by a nearest neighbor pixel. The resonance at 3 kHz is a consequence of the frequency shift algorithm, used to move the intermodulation distortions at 1.5 kHz and higher harmonics in the demodulated TES response. The excess noise within $G(1 + \mathcal{L}_0)/2\pi C \simeq 240$ Hz (thermal bandwidth) in the blue curve is a sign of thermal crosstalk.

We calculate the integrated NEP ΔE_0 from the fundamental noise power spectrum, defined from the noise events acquired when no X-ray events are detected in any active TES and then compare it to the integrated NEP ΔE_{TCT} obtained by adding in quadrature to the fundamental noise the power spectrum of the average TCT pulse. Given the low signal-to-noise ratio of the TCT, to avoid overestimations, we first subtract the contribution of the fundamental noise from the average TCT pulse power spectrum. In Fig. 7, left plot, we show an example of fundamental NEP spectrum and the contribution of TCT to the NEP spectrum. The impact on spectral performance is then estimated as

$$\sqrt{\Delta E_{\mathrm{TCT}}^2 - \Delta E_0^2}. \quad (4)$$

For nearest neighbor pixels lying along the direction with no-metallization muntins, such value is of the order of 10 meV and is significantly lower for pixels lying along the direction of Cu-plated muntins.
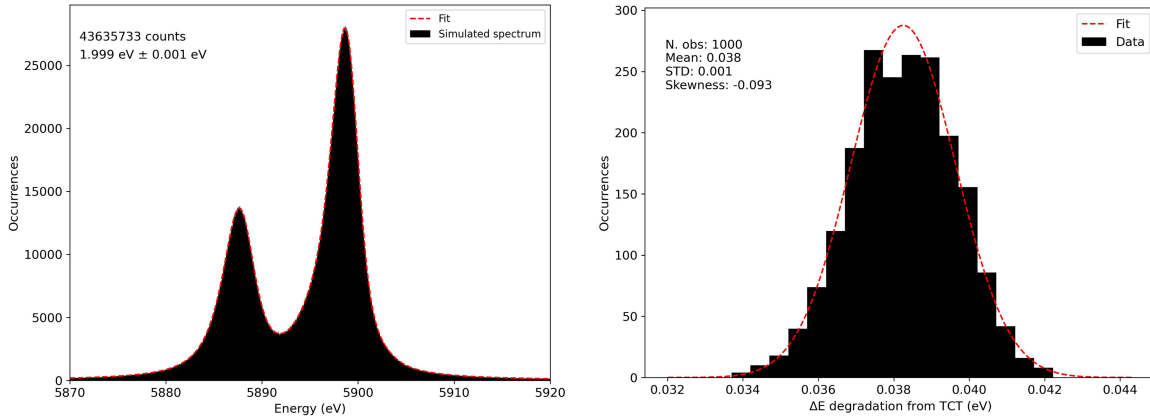
Fig. 8.   Left: simulated energy spectrum for the Mn-K α lines of a ^{55}Fe X-ray Perpetrator. The extreme number of simulated events is necessary to reduce the statistical error to 1 meV since from the NEP estimation, we expect the impact on resolution to be of the order of at least 10 meV. Right: histogram of the degradation in quadrature caused by random TCT in the simulated spectrum for 1000 observations.

This method considers the increased phonon noise in the Victim pixel caused by thermal disturbances from one Perpetrator pixel; however, it is not representative for an actual FDM multipixel configuration, with multiple Perpetrators surrounding the Victim and an increased effective count rate. Therefore, we consider the impact on performance measured in this way as an underestimation. To make a more realistic assessment, we use a Monte Carlo simulation.

2) Monte Carlo Simulation: In this approach, we simulate an X-ray spectrum composed by the Mn-K α and Mn-Kβ lines as typically measured from the ^{55}Fe source in our experimental setups. To do so, we take random samples from a probability distribution constructed using the natural line data and branching ratios present in the study by Holzer *et al.* [18], convolved with a Gaussian function to tune the resolution of the K$\alpha_{1,2}$ lines to a value of 2 eV. The spectral performance is estimated by fitting the Mn-K$\alpha_{1,2}$ model to the simulated data using the Cash-statistics [19] in the maximum-likelihood method. We simulate the energy spectrum with a number of events large enough to reduce the statistical error of the fit to 1 meV (one order of magnitude lower than the impact estimated by NEP approach), as shown in Fig. 8, left plot.

We then contaminate the simulated spectrum with TCT events. For the contamination to happen, an X-ray should release energy in the Perpetrator within a time window δ equal to the entire relaxation time of the Victim X-ray pulse, which we can consider to be of the order of 10 ms, as shown in Fig. 4, right plot. Considering a typical count rate ν for each pixel of ∼1 Hz, the probability of having an X-ray event in one pixel follows a Poisson distribution with mean $\nu\delta$. The probability of two concurrent, independent events in the Perpetrator and Victim pixel is then given by the product of the two individual probabilities. Considering that each Victim has N_P neighbor Perpetrator pixels, the contamination probability is calculated as

$$P_{\text{TCT}} = \left(\nu\delta e^{-\nu\delta}\right)\bigg|_V \sum_{N_P}\left(\nu\delta e^{-\nu\delta}\right)\bigg|_S = N_P\left(\nu\delta e^{-\nu\delta}\right)^2. \quad (5)$$

Considering $\delta = 10$ ms, $\nu = 1$ Hz, and $N_P = 8$ (assuming the TCT of higher-than-$\sqrt{2}$ neighbors to be negligible), we get $P_{\text{TCT}} \approx 7.8 \times 10^{-4}$. To perform a random TCT contamination, for each event of the simulated spectrum, we generate a random number X within 0 and 1 with a uniform probability distribution.

Then, if the condition $X < P_{\text{TCT}}$ is verified, we sum the TCT contribution ϵ to the energy E_0 of the X-ray event. To calculate ϵ, we consider the weighted average of the energy for Mn-Kα X-rays ≈ 5895 eV and a CR of 10^{-4} so that the average energy for TCT pulse $\epsilon \approx 0.6$ eV. This is a conservative estimation since the average CR for first neighbors is 9×10^{-5} and it is expected to be even better with an improved, uniform Cu metallization.

In this way, we construct a "contaminated" spectrum, which we fit to extract the energy resolution of the Mn-Kα lines. The degradation (in quadrature) coming from TCT is then calculated according to (4).

To assess the expected impact of TCT on spectral resolution, we repeat this process for a large number of observations (i.e., random contamination of the simulated spectrum and calculation of the degradation in quadrature). In Fig. 8, right plot, we show the results of the simulation for one thousand observations. By fitting the data with a Gaussian distribution, we find an average impact of 0.038 eV $\pm$ 0.001 eV, larger than the value from NEP estimation, as expected. This value is significantly lower than the system requirements for Athena X-IFU, whose energy resolution budget for TCT is 0.2 eV, considering an instrumental energy resolution of 2.5 eV in the energy range of 0.2-7 keV for count rates per pixel of the order of 1 Hz [20].

V. Conclusion

We presented a characterization of TCT for two TES arrays performed in two setups for FDM readout of TES X-ray microcalorimeters. Both the readout system and the TES arrays under study were produced at SRON. The measured level of TCT is consistent between the two setups and is within the requirements for Athena X-IFU, with the highest CRs for nearest neighbor pixels of 1.4×10^{-4} for the 8×8 array, and 4.3×10^{-4} for the central region and 1.6×10^{-4} at the edge of the kilo-pixel array. The CRs appear to be well below 10^{-4} if the direction along the Cu muntin is considered.

By comparing the integrated NEP with and without the contribution due to the TCT, we estimated the impact on energy resolution and the energy of the TCT pulse for each Perpetrator–Victim combination. Using this information, we run a Monte Carlo simulation to estimate the degradation in quadrature in representative conditions for multipixel readout. In this way, we estimate an average impact of approximately 40 meV for a count

rate per pixel of 1 Hz, compatible with the energy resolution budget allocated for TCT in Athena X-IFU.

These results indicate that the TCT level for our TES arrays as measured in our FDM-based system is suitable for future spaceborne X-ray missions. Despite the impact of TCT being already acceptable, we envisage the possibility to further reduce it by improving the metallization process of the silicon muntin and increasing the muntin width from 60 to 85 μm in future batches of arrays and have a better thermalization for the TES array by using thicker or ribbon Au wire bondings.

DATA AVAILABILITY

The corresponding author makes available the data presented in this article upon reasonable request.

REFERENCES

[1] K. D. Irwin and G. C. Hilton, "Transition-edge sensors," in *Cryogenic Particle Detection*, vol. 99. Berlin, Germany: Springer, 2005, pp. 63–150.

[2] H. Sugai *et al.*, "Updated design of the CMB polarization experiment satellite LiteBIRD," *J. Low Temp. Phys.*, vol. 199, no. 3, pp. 1107–1117, 2020.

[3] W. Cui *et al.*, "HUBS: Hot universe baryon surveyor," *J. Low Temp. Phys.*, vol. 199, no. 1-2, pp. 502–509, 2020.

[4] D. Barret *et al.*, "The Athena X-ray integral field unit (X-IFU)," in *Proc. Space Telescopes Instrum. 2016: Ultraviolet Gamma Ray*, 2016, Art. no. 99052F.

[5] R. den Hartog *et al.*, "Baseband feedback for frequency domain multiplexed readout of TES X-ray detectors," *API Conf. Proc.*, vol. 1185, no. 1, pp. 261–264, 2009.

[6] H. Akamatsu *et al.*, "Demonstration of 37-pixel frequency domain multiplexing readout of cryogenic X-ray microcalorimeters," *Appl. Phys. Lett.*, vol. 119, 2021, Art. no. 182601, doi: 10.1109/TASC.2021.3128710.

[7] K. Nagayoshi *et al.*, "Development of a Ti/Au TES microcalorimeter array as a backup sensor for the Athena/X-IFU instrument," *J. Low Temp. Phys.*, vol. 199, no. 3, pp. 943–948, 2020.

[8] M. de Wit *et al.*, "High aspect ratio transition edge sensors for X-ray spectrometry," *J. Appl. Phys.*, vol. 128, no. 22, 2020, Art. no. 224501.

[9] M. P. Bruijn, L. Gottardi, R. H. den Hartog, J. van der Kuur, A. J. van der Linden, and B. D. Jackson, "Tailoring the high-Q LC filter arrays for readout of kilo-pixel TES arrays in the SPICA-SAFARI instrument," *J. Low Temp. Phys.*, vol. 176, pp. 421–425, 2014.

[10] L. Gottardi *et al.*, "A six-degree-of-freedom micro-vibration acoustic isolator for low-temperature radiation detectors based on superconducting transition-edge sensors," *Rev. Sci. Instrum.*, vol. 90, 2019, Art. no. 055107.

[11] E. Taralli *et al.*, "Ti/Au TES 32 × 32 pixel array: Uniformity, thermal crosstalk and performance at different X-ray energies," *IEEE Trans. Appl. Supercond.*, vol. 31, no. 5, Aug. 2021, Art. no. 2100605.

[12] P. van der Hulst *et al.*, "Frequency shift algorithm: Design of a baseband phase locked loop for frequency-domain multiplexing readout of X-ray transition-edge sensor microcalorimeters," *Review of Scientific Instruments*, vol. 92, 2021, Art. no. 073101, doi: 10.1063/5.0044968.

[13] D. Vaccaro *et al.*, "Frequency shift algorithm: Application to a frequency-domain multiplexing readout of X-ray transition-edge sensor microcalorimeters," *Rev. Sci. Instrum.*, vol. 92, 2021, Art. no. 033103.

[14] N. Iyomoto *et al.*, "Heat sinking and crosstalk for large, close-packed arrays of microcalorimeters," *J. Low Temp. Phys.*, vol. 151, pp. 506–512, 2008.

[15] A. R. Miniussi *et al.*, "Thermal crosstalk measurements and simulations for an X-ray microcalorimeter array," *J. Low Temp. Phys.*, vol. 199, pp. 1–9, 2020.

[16] L. Gottardi *et al.*, "Weak-link phenomena in AC-biased transition edge sensors," *J. Low Temp. Phys.*, vol. 176, pp. 279–284, 2014.

[17] N. Iyomoto *et al.*, "Heat sinking, crosstalk, and temperature uniformity for large close-packed microcalorimeter arrays," *IEEE Trans. Appl. Supercond.*, vol. 19, no. 3, pp. 557–560, Jun. 2009.

[18] G. Hölzer, M. Fritsch, M. Deutsch, J. Härtwig, and E. Förster, "$K\alpha_{1,2}$ and $K\beta_{1,3}$ emission lines of the 3 d transition metals," *Phys. Rev.*, vol. 56, 1997, Art. no. 4554.

[19] J. S. Kaastra, "On the use of C-stat in testing models for X-ray spectra," *Astron. Astrophys.*, vol. 605, 2017, Art. no. A51.

[20] P. Peille *et al.*, "The performance of the athena X-ray integral field unit at very high count rates," *J. Low Temp. Phys.*, vol. 193, pp. 940–948, 2018.